Green Chemistry

COMMUNICATION

View Article Online
View Journal | View Issue

Cite this: *Green Chem.*, 2017, **19**, 4284

Received 11th April 2017,
Accepted 7th August 2017

DOI: 10.1039/c7gc01095h

rsc.li/greenchem

Composition-tunable synthesis of "clean" syngas *via* a one-step synthesis of metal-free pyridinic-N-enriched self-supported CNTs: the synergy of electrocatalyst pyrolysis temperature and potential†

Kai-Hua Liu,[a,b] Hai-Xia Zhong,[b] Xiao-Yang Yang,[a,b] Di Bao,[b] Fan-Lu Meng,[a,b] Jun-Min Yan *[a] and Xin-Bo Zhang [b]

Exploring efficient and environmentally friendly ways for producing clean syngas is of great significance for realizing an artificial carbon cycle associated with clean and renewable energy. Herein, as a proof-of-concept experiment, we controllably synthesized syngas *via* electroreduction of CO_2 using an integrated 3D electrode as the catalyst. An efficient electrode was synthesized in only one step and immediately used for electroreduction of CO_2 to CO with a low overpotential. Moreover, pyridinic-N predominated in the synthesized N-CNTs, followed by graphitic-N, both of which were demonstrated to supply the active nitrogen defects for the CO_2 conversion. Impressively, by tuning the pyrolysis temperature or applied potential, we were able to easily tailor the H_2/CO ratio in the clean syngas products in a large range between 1 : 3 and 3 : 1. This ability to tailor the H_2/CO ratio has important applications in industrial production.

Syngas, a mixture of H_2 and CO, is usually used as the intermediate for producing methane, methanol and synthetic hydrocarbon fuels, and different industrial applications require different ratios of H_2 to CO.[1,2] Currently, production of syngas is mainly carried out *via* the steam reforming of natural gas or the gasification of coal, which requires harsh synthesis conditions, such as high temperature and pressure, and releases a large number of by-products, inevitably aggravating the energy and environmental crisis.[3] Moreover, this conventional syngas preparation cannot well control the ratio of the syngas components, and a subsequent adjustment is therefore needed. In this regard, CO_2 is an ideal feedstock for syngas production. And among the many advanced CO_2 conversion methods, electroreduction of CO_2, coupled with the use of renewable energy, is a particularly promising and appealing strategy to achieve a carbon-neutral energy cycle under mild conditions.[4–7] However, this conversion reaction is largely impeded by the sluggish reactivity of the relatively stable CO_2 molecule and by the competing hydrogen evolution reaction (HER) that occurs at a similar potential range, and hence highly efficient catalysts for the conversion reaction are urgently required.[8–11] Although precious metals such as silver and gold can selectively convert CO_2 to CO, they are not suitable for practical applications because of their scarcity and high costs.[12] And the high overpotential, low faradaic efficiency and selectivity as well as questionable stability of catalysts based on non-precious transition metals hinder their wide application in the conversion reaction.[13,14] Therefore, it is highly desirable albeit a challenge to explore optimized and low-cost electrocatalysts for CO_2 reduction to directly acquire the specific ratios of the H_2 and CO syngas components required industrially.

Nanocarbon-based materials, especially nitrogen-doped carbon nanotubes (N-CNTs), have attracted increasing research interest[15] because of their distinct properties, such as high surface area, outstanding conductivity, excellent chemical stability, remarkable mechanical strength,[16] and inferior HER activity. Conventionally, N-CNTs are synthesized by using the liquid chemical vapor deposition method, which requires costly equipment and a high temperature as well as a special or toxic atmosphere.[15,17,18] Thus, it is compelling to search for inexpensive and facile methods to synthesize N-CNTs, particularly those with abundant and active nitrogen defects. Moreover, most catalysts need to be immobilized on planar substrates (*e.g.*, glass carbon) using a polymer binder (*e.g.*, Nafion),[19] and this process is time-consuming and expensive. Importantly, the binder inevitably buries active sites and blocks the mass/electron transport, and thus deteriorates the electrocatalytic activity.[20] Furthermore, the glued catalysts fall off the substrate too often because of the vigorous gas bubbling, worsening their stability. Also, the process of drying the catalyst on the substrate leaves the catalyst in a dehydrated form, which leads to poor wettability and a limited number of accessible active sites.[21,22] Thus, the development of a strategy

[a]*Key Laboratory of Automobile Materials, Ministry of Education and College of Materials Science and Engineering, Jilin University, Changchun 130012, China. E-mail: junminyan@jlu.edu.cn*
[b]*State Key Laboratory of Rare Earth Resource Utilization, Changchun Institute of Applied Chemistry, Chinese Academy of Sciences, Changchun 130022, China*
†Electronic supplementary information (ESI) available. See DOI: 10.1039/c7gc01095h

involving directly integrating active materials with current collectors to fabricate an integrated electrode is highly desirable.[23–26] A three-dimensional (3D) porous integrated electrode may be the ideal choice for achieving an improved electroactive surface area with more exposed active sites and accelerated mass transport.[27] Therefore, there is an urgent need to develop a facile and effective means to construct a 3D integrated electrode for CO_2 electroreduction to obtain syngas with high activity and stability but at low cost, although such a pursuit is a great challenge.

With these purposes in mind, we herein, as a proof-of-concept experiment, synthesized an integrated 3D electrode with N-CNTs directly grown on a stainless steel mesh (N-CNTs/SS), and this electrode was directly used to reduce CO_2 and obtain clean syngas. Here, the SS not only acted as a scaffold for integrating the N-CNTs and current collector, but also as a self-catalytic substrate for growing CNTs without any pretreatment. Furthermore, melamine was used as the carbon and nitrogen sources, ensuring optimized nitrogen doping. Satisfactorily, pyridinic-N predominated in the synthesized N-CNTs, followed by graphitic-N, which are both active nitrogen defects for CO_2 conversion. Finally, this electrode showed high catalytic activity for the production of clean and various ratios of the syngas components, a high Faradaic efficiency (FE) of 75% for CO, and superior durability. By changing the synthesis conditions or applied voltage, we were able to finely tailor the H_2/CO product ratio, a benefit for practical applications.

The integrated 3D N-CNTs/SS electrode was facilely fabricated as shown in Fig. 1a. Briefly, the N-CNTs were *in situ* grown on SS under an inert atmosphere, wherein melamine was used as both the nitrogen and carbon sources. As shown in Fig. 1b and c, the surfaces of N-CNTs/SS were uniformly and densely packed with N-CNTs, quite different from the relatively smooth surface of bare SS. Note that the morphology of the N-CNTs varied with different pyrolysis temperatures. N-CNTs grown at a low temperature were thick and short. As the temperature was increased to 750 °C, the N-CNTs became thinner and longer. But as the temperature was further increased, the SS became fragile and folded (Fig. S1 and S3†). So the synthesized N-CNTs/SS at 750 °C (N-CNTs/SS-750) exhibited the optimal morphology. The energy dispersive X-ray spectroscopy (EDX) element mapping identified the presence of the elements C and N (Fig. 1d), which were homogeneously distributed along the whole structure. Furthermore, the typical transmission electron microscopy (TEM) images showed N-CNT to have a multiwall structure with diameters of about 100 nm. A lattice fringe of 0.337 nm was observed, and was ascribed to the carbon (002) (Fig. 2a). The element mapping image also showed N to be uniformly distributed throughout the observed N-CNT (Fig. 2b).

Meanwhile, structural characterizations were also performed using Raman spectroscopy and X-ray diffraction (XRD). The Raman spectra of the synthesized N-CNTs included two obvious characteristic peaks corresponding to the D band (1360 cm^{-1}) and G band (1590 cm^{-1}) (Fig. 2c). The D band is

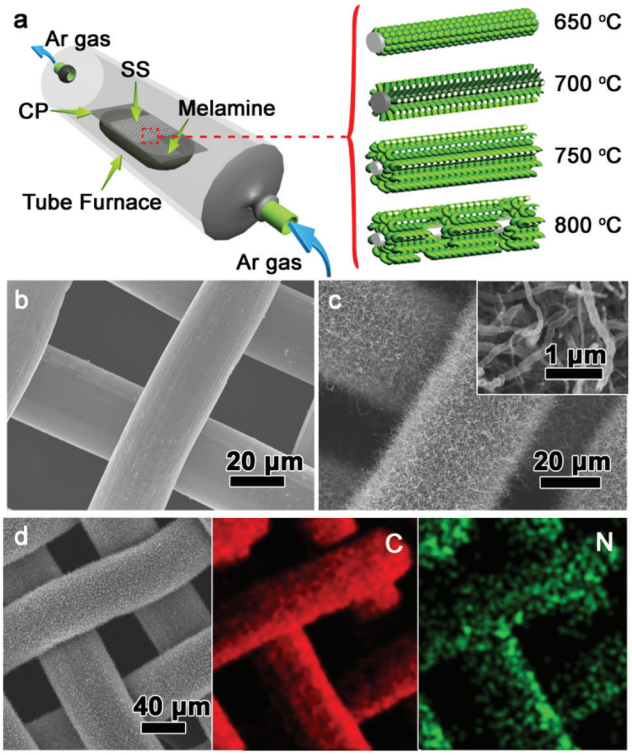

Fig. 1 (a) Schematic of the procedure used to synthesize the N-CNTs/SS. (b, c) SEM images of (b) pure SS and (c) synthesized N-CNTs/SS. (d) SEM EDS element mapping images of C and N for N-CNTs/SS-750.

indicative of a series of defects caused by the doping effect while the G band is related to the in-plane bond-stretching motion of pairs of sp^2 carbon atoms.[28] Note that N-CNTs/SS-750 showed a higher value of I_D/I_G (1.01) than did N-CNTs/SS-650 (0.93), N-CNTs/SS-700 (0.95), and N-CNTs/SS-800 (0.94), indicating its greater number of defects. All of these I_D/I_G values were found to be higher than that of pristine commercial CNTs (I_D/I_G = 0.58) as shown in Fig. S4,† and these greater values were associated with the introduction of nitrogen defects. The X-ray diffraction (XRD) patterns of the synthesized N-CNTs/SS-750 showed an obvious carbon peak (002) (Fig. S5†), consistent with the TEM results. The other component analysis is shown in Fig. S6.†

In addition, X-ray photoelectron spectroscopy (XPS) measurements were taken to probe the nitrogen concentration and atomic configuration of N-CNTs. As shown in Fig. 2d, the C 1s region of the high-resolution spectrum of N-CNTs was fitted by several single peaks, specifically those corresponding to C=C (284.5 eV), C=N (285.2 eV), C–N (286.2 eV) and C–O (286.7 eV), further confirming the successful doping of N into the CNTs.[29] And the N 1s region of the spectrum was fitted by peaks centered at 398.4, 399.9, and 401.1 eV, indicating the discovery of three different bonding states of N in the N-CNTs, *i.e.*, pyridinic-N (N1), pyrrolic-N (N2), and graphitic-N (N3), respectively (Fig. 2e and S7†).[30] The N-CNTs/SS-750 showed the highest total N content (~6.8 atom %) based on the N/(N + C) atomic ratio and the pyridinic-N content of ~3.9 atom %. The

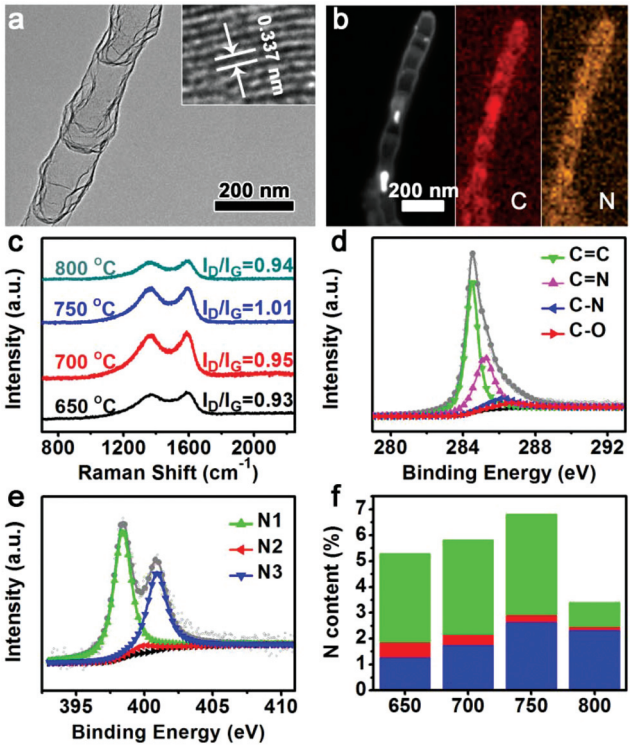

Fig. 2 (a) TEM image of N-CNTs/SS-750 (inset: HRTEM image of N-CNT). (b) Element mapping images of C and N for a single N-CNT. (c) Raman spectrum of N-CNTs/SS with different pyrolysis temperatures. (d, e) High-resolution XPS spectra of N-CNTs/SS-750 in the (d) C 1s and (e) N 1s regions. (f) N contents of N-CNTs/SS-750 with different synthesis temperatures.

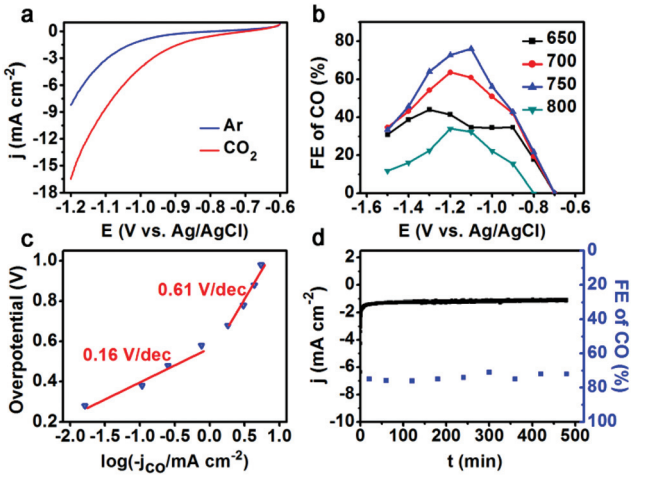

Fig. 3 CO_2 electroreduction performances. (a) Linear sweep voltammetric curves of N-CNTs/SS-750 in Ar- and CO_2-saturated 0.1 M $KHCO_3$ electrolytes. (b) Faradaic efficiencies for CO at various applied potentials. (c) Tafel plots based on *Jco* for N-CNTs/SS-750. (d) Chronoamperometric responses and the corresponding faradaic efficiency of N-CNTs/SS-750 at −1.1 V *vs.* Ag/AgCl.

initial temperature increase was beneficial for the growth of N-CNTs, as can be seen from the SEM images (Fig. S3†), and caused an increase of total N content. And then the total N content decreased as the temperature was further increased because the N-CNTs became short and due to the instability of pyrrolic-N and pyridinic-N, consistent with previous reports.[31] Moreover, the pyridinic-N was found to predominate in N-CNTs/SS-650, N-CNTs/SS-700 and N-CNTs/SS-750. In addition, this trend in total N content was also indicated by elemental analysis (Table S1†).

The electrochemical activities of the synthesized electrodes were first evaluated by taking linear sweep voltammetry measurement in Ar- and CO_2-saturated $KHCO_3$ solutions. As shown in Fig. 3a, the current densities recorded when using the Ar-saturated electrolyte were due to the evolution of hydrogen, and showed a high onset potential of about −0.9 V *vs.* Ag/AgCl. The potentials in this work were reported *versus* Ag/AgCl except when indicated otherwise. Compared to the Ar-saturated electrolyte, the electrolyte saturated with CO_2 yielded higher-magnitude cathode current densities over the entire potential range and showed a more positive onset potential of −0.8 V, which might have been associated with the occurrence of the CO_2 reduction reaction. And as shown in Fig. S8,† N-CNTs/SS-750 exhibited the highest catalytic activity among the four samples, with greater current densities and a more positive onset potential. The electrochemical surface areas were evaluated by estimating the double-layer capacitance (C_{dl}) values from cyclic voltammograms acquired using different scan rates. As shown in Fig. S9,† the C_{dl} of N-CNTs/SS-750 was measured to be 8.3 mF cm^{-2}, a value greater than those of the other samples. This result showed that of all the samples, N-CNTs/SS-750 had the largest active surface area, which apparently provided it with the most catalytically active sites, and hence accounted for its superior catalytic activity.

As selectivity is also an important parameter for evaluating the CO_2 reduction electrocatalysts, the gas and liquid products were analyzed by carrying out gas chromatography and ^1H nuclear magnetic resonance spectroscopy experiments. Only gas products, mainly H_2 and CO along with an extremely low amount of CH_4, were detected at the cathode side (Fig. S10 and S11†). Note that these gases are the main components of syngas. As shown in Fig. S12,† the partial current density levels of CO for all N-CNTs/SS samples were observed to increase as the applied potential was increased. In contrast, the FE for CO of N-CNTs/SS synthesized at different temperatures increased as the potential was increased to −1.1 V, and gradually decreased as the potential was increased further (Fig. 3b), which may have been due to the competition between the HER and CO_2 reduction. And N-CNTs/SS-750 showed an obviously larger partial current density for CO than did N-CNTs/SS-650, N-CNTs/SS-700 and N-CNTs/SS-800, demonstrating its superior catalytic activity. The higher catalytic activity of N-CNTs/SS-750 was also indicated by its reduction of CO_2, which produced CO starting at an overpotential of −0.09 V (*vs.* RHE) with an FE of ~22%. Meanwhile, the maximum FE displayed by N-CNTs/SS-750 for CO was ~75%, which occurred at a low overpotential of −0.39 V (*vs.* RHE), whereas the

maximum FE values displayed by N-CNTs/SS-700, N-CNTs/SS-650, and N-CNTs/SS-800 were 63%, 44%, and 33%, respectively, further highlighting the better performance of N-CNTs/SS-750, which also outperformed many other catalysts reported so far (Tables S2†). Its superior catalytic activity may have been due to its abundant active sites and pores, excellent conductivity (Fig. S13†), and it having the lowest interfacial charge-transfer resistance of all the tested samples, which indicates a rapid electron transfer during the reduction process as shown in Fig. S14.† Additionally, relatively little CH_4 was found at high overpotential in the presence of N-CNTs/SS-750, with the FE below ~1% (Fig. S15†). For comparison, we also tested CO_2 reduction on pristine SS under otherwise the same conditions: no CO was detected (Fig. S11a†), similar to the results of the N-CNTs/SS-750 electrode electrolysis in an Ar-saturated electrolyte (Fig. S11b†), and confirming that it was the N-CNTs that mainly contributed to the enhancement of the catalysis of the CO_2 reduction.

To obtain further insights into the catalytic activity of N-CNTs/SS, the kinetics for CO formation was extracted from Tafel plots (Fig. 3c and S16†). The Tafel slope at low overpotential for the N-CNTs/SS-750 catalyst was determined to be 0.16 V dec^{-1}, lower than those determined for the other catalysts, indicating the rate of CO formation was greatest in the presence of N-CNTs/SS-750. The Tafel slope for N-CNTs/SS-750 increased to 0.61 V dec^{-1} at high overpotential, which might have been due to the change of adsorbed species on the electrode surface or the limit of electron transfer, and implies there is a change in the rate-determining step.[17,32]

Besides the CO_2 reduction activity, electrochemical stability is another important criterion to assess the suitability of an advanced electrocatalyst for practical applications. Thus, chronoamperometric responses were performed at −1.1 V for 8 h in a CO_2-saturated electrolyte. In the presence of N-CNTs/SS-750, there was negligible decay of the current density under continuous operation, and the FE for producing CO was always greater than 70% during the long test period, indicative of the very high stability of the electrode (Fig. 3d). A comparison of an SEM image and XRD pattern of N-CNTs/SS-750 after the stability test (Fig. S17†) with those beforehand showed negligible change in the morphology and structure, demonstrating the durable 3D structure of this integrated electrode. The high stability and other attributes of N-CNTs/SS indicate it to be a promising catalyst for electrocatalytic CO_2 conversion.

Notably, the ratio of H_2 to CO can be controlled by selecting the synthesis temperature of N-CNTs/SS and the applied potential. Different ratios of these components of syngas are ideal for different fuel product applications, such as methanation, the Fischer–Tropsch (F–T) process and hydroformylation.[33] The pyrolysis temperature used was found to affect the nitrogen content and nitrogen type, and hence to influence the selectivity of CO_2 reduction or the ratio of H_2 to CO. As shown in Fig. 4a and b, the ratio of H_2 to CO was found to be correlated with the content of pyridinic-N. For example, at temperatures below 750 °C, the pyridinic-N content gradually increased with increasing temperature, resulting in a decrease

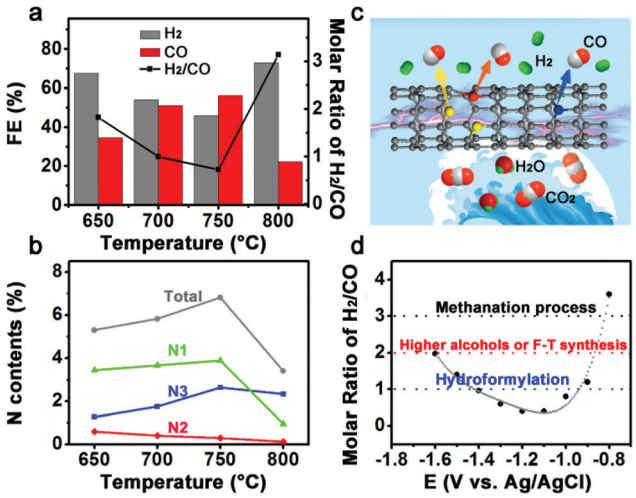

Fig. 4 (a) Faradaic efficiency and molar ratio of H_2/CO of different samples at −1.0 V *vs.* Ag/AgCl. (b) N contents of the different samples. (c) Scheme for the electroreduction of CO_2 and H_2O into syngas on an N-CNT. (d) Industrial applications of different ratios of H_2/CO *versus* the applied potential.

in the ratio of H_2 to CO from 2 to 1 at the same potential of −1.0 V. Syngas with an H_2-to-CO ratio of 2 can be used to synthesize methanol or ethanol or light olefins when using the F–T process ($nCO + 2nH_2 \rightarrow [-CH_2-]_n + nH_2O$).[34] And syngas with an H_2-to-CO ratio of 1 can be used to synthesize aldehydes by carrying out a hydroformylation of alkenes.[35] The ratio of H_2 to CO produced in the presence of N-CNTs/SS-800 was 3, which can be used to synthesize methane when carrying out the methanation process ($3H_2 + CO \rightarrow CH_4 + H_2O$).[35] These results all illustrated that pyridinic-N plays a decisive role in the selectivity of CO_2 reduction and the components of syngas produced (the ratio of H_2 to CO). In addition, the correlation between catalytic activity and the type of N-defect is shown in Fig. S18.† Apart from tuning the calcinating temperature, the ratio of the syngas components can also be tailored by only changing the applied potential as shown in Fig. 4d.

We have shown that various ratios of the components of clean syngas can be directly acquired by only changing the pyrolysis temperature or applied potential. Considering the overpotential and stability, a synergistic effect of pyrolysis temperature and applied potential should be considered to obtain the desired ratio of the syngas components. Syngas with an H_2-to-CO ratio of 1 and 3 can be obtained at potentials of −0.9 V and −0.8 V for N-CNTs/SS-750, and a ratio of 2 can be acquired at −1 V for N-CNTs/SS-650.

Conclusions

In summary, as a proof-of-concept experiment, a 3D integrated N-CNTs/SS electrode was facilely fabricated by growing N-CNTs *in situ* on the SS with only melamine as the nitrogen and carbon sources, avoiding the use of a toxic gas. This integrated

electrode displayed efficient, durable and controllable clean syngas production from CO_2 reduction as well as a high FE of 75% for CO. Impressively, the H_2/CO ratio in the clean syngas product can be easily tailored in a large range between 1 : 3 and 3 : 1 by tuning the pyrolysis temperature or applied potential. Such an integrated and cost-effective electrode makes the CO_2 reduction proceed in a more direct and efficient manner, reducing the production cost. We anticipate that the successful design of such an integrated electrode will lead to improved means to develop more economical and efficient 3D integrated structured electrodes for the syngas industry and other useful carbon products.

Conflicts of interest

There are no conflicts to declare.

Acknowledgements

This work was financially supported by National Natural Science Foundation of China (51522101, 51471075, 5163100, and 51401084); and Specialized Research Fund for the Doctoral Program of Higher Education of China (20110061120040).

Notes and references

1 S. Chu, S. Fan, Y. Wang, D. Rossouw, Y. Wang, G. A. Botton and Z. Mi, *Angew. Chem., Int. Ed.*, 2016, **55**, 14262–14266.
2 Q. Lu, J. Rosen, Y. Zhou, G. S. Hutchings, Y. C. Kimmel, J. G. Chen and F. Jiao, *Nat. Commun.*, 2014, **5**, 3242.
3 X. Zou and Y. Zhang, *Chem. Soc. Rev.*, 2015, **44**, 5148–5180.
4 S. Gao, X. Jiao, Z. Sun, W. Zhang, Y. Sun, C. Wang, Q. Hu, X. Zu, F. Yang, S. Yang, L. Liang, J. Wu and Y. Xie, *Angew. Chem., Int. Ed.*, 2016, **55**, 698–702.
5 W.-H. Wang, Y. Himeda, J. T. Muckerman, G. F. Manbeck and E. Fujita, *Chem. Rev.*, 2015, **115**, 12936–12973.
6 J. Qiao, Y. Liu, F. Hong and J. Zhang, *Chem. Soc. Rev.*, 2014, **43**, 631–675.
7 S. Gao, Y. Lin, X. Jiao, Y. Sun, Q. Luo, W. Zhang, D. Li, J. Yang and Y. Xie, *Nature*, 2016, **529**, 68–71.
8 A. J. Martín, G. O. Larrazábal and J. Pérez-Ramírez, *Green Chem.*, 2015, **17**, 5114–5130.
9 A. Nakada, K. Koike, K. Maeda and O. Ishitani, *Green Chem.*, 2016, **18**, 139–143.
10 J.-Y. Liu, B. Garg and Y.-C. Ling, *Green Chem.*, 2011, **13**, 2029–2031.
11 Z. Weng, J. Jiang, Y. Wu, Z. Wu, X. Guo, K. L. Materna, W. Liu, V. S. Batista, G. W. Brudvig and H. Wang, *J. Am. Chem. Soc.*, 2016, **138**, 8076–8079.
12 D. H. Won, H. Shin, J. Koh, J. Chung, H. S. Lee, H. Kim and S. I. Woo, *Angew. Chem., Int. Ed.*, 2016, **55**, 9297–9300.
13 Y. Chen, C. W. Li and M. W. Kanan, *J. Am. Chem. Soc.*, 2012, **134**, 19969–19972.
14 Y. Liu, S. Chen, X. Quan and H. Yu, *J. Am. Chem. Soc.*, 2015, **137**, 11631–11636.
15 J. Wu, R. M. Yadav, M. Liu, P. P. Sharma, C. S. Tiwary, L. Ma, X. Zou, X.-D. Zhou, B. I. Yakobson, J. Lou and P. M. Ajayan, *ACS Nano*, 2015, **9**, 5364–5371.
16 D. D. Zhu, J. L. Liu and S. Z. Qiao, *Adv. Mater.*, 2016, **28**, 3423–3452.
17 P. P. Sharma, J. Wu, R. M. Yadav, M. Liu, C. J. Wright, C. S. Tiwary, B. I. Yakobson, J. Lou, P. M. Ajayan and X.-D. Zhou, *Angew. Chem., Int. Ed.*, 2015, **54**, 13701–13705.
18 K. P. Gong, F. Du, Z. H. Xia, M. Durstock and L. M. Dai, *Science*, 2009, **323**, 760–764.
19 H. Wang, Y. Chen, X. Hou, C. Ma and T. Tan, *Green Chem.*, 2016, **18**, 3250–3256.
20 J. Wang, H.-X. Zhong, Z.-L. Wang, F.-L. Meng and X.-B. Zhang, *ACS Nano*, 2016, **10**, 2342–2348.
21 S. Chen, J. J. Duan, M. Jaroniec and S. Z. Qiao, *Angew. Chem., Int. Ed.*, 2013, **52**, 13567–13570.
22 H. Zhong, J. Wang, F. Meng and X. Zhang, *Angew. Chem., Int. Ed.*, 2016, **55**, 9937–9941.
23 Z. Lu, W. Zhu, X. Yu, H. Zhang, Y. Li, X. Sun, X. Wang, H. Wang, J. Wang, J. Luo, X. Lei and L. Jiang, *Adv. Mater.*, 2014, **26**, 2683–2687.
24 P. Jiang, Q. Liu, Y. Liang, J. Tian, A. M. Asiri and X. Sun, *Angew. Chem., Int. Ed.*, 2014, **53**, 12855–12859.
25 J. Wang, H.-x. Zhong, Y.-l. Qin and X.-b. Zhang, *Angew. Chem., Int. Ed.*, 2013, **52**, 5248–5253.
26 D. S. Kong, H. T. Wang, Z. Y. Lu and Y. Cui, *J. Am. Chem. Soc.*, 2014, **136**, 4897–4900.
27 J. Jiang, Y. Li, J. Liu, X. Huang, C. Yuan and X. W. Lou, *Adv. Mater.*, 2012, **24**, 5166–5180.
28 S. Zhang, P. Kang, S. Ubnoske, M. K. Brennaman, N. Song, R. L. House, J. T. Glass and T. J. Meyer, *J. Am. Chem. Soc.*, 2014, **136**, 7845–7848.
29 Z.-H. Sheng, L. Shao, J.-J. Chen, W.-J. Bao, F.-B. Wang and X.-H. Xia, *ACS Nano*, 2011, **5**, 4350–4358.
30 J. Liang, Y. Jiao, M. Jaroniec and S. Z. Qiao, *Angew. Chem., Int. Ed.*, 2012, **51**, 11496–11500.
31 T. Sharifi, G. Hu, X. Jia and T. Wagberg, *ACS Nano*, 2012, **6**, 8904–8912.
32 R. Kas, K. K. Hummadi, R. Kortlever, P. de Wit, A. Milbrat, M. W. J. Luiten-Olieman, N. E. Benes, M. T. M. Koper and G. Mul, *Nat. Commun.*, 2016, **7**, 10748.
33 S. R. Foit, I. C. Vinke, L. G. J. de Haart and R.-A. Eichel, *Angew. Chem., Int. Ed.*, 2017, **56**, 5402–5411.
34 L. Zhong, F. Yu, Y. An, Y. Zhao, Y. Sun, Z. Li, T. Lin, Y. Lin, X. Qi, Y. Dai, L. Gu, J. Hu, S. Jin, Q. Shen and H. Wang, *Nature*, 2016, **538**, 84–87.
35 H. Mistry, R. Reske, Z. Zeng, Z. J. Zhao, J. Greeley, P. Strasser and B. R. Cuenya, *J. Am. Chem. Soc.*, 2014, **136**, 16473–16476.

